Publ. Astron. Soc. Japan (2014) 00(0), 1–12
doi: 10.1093/pasj/xxx000

The Subaru FMOS Galaxy Redshift Survey (FastSound). I. Overview of the Survey Targeting on Hα Emitters at $z \sim 1.4$

**Motonari TONEGAWA,[1] Tomonori TOTANI,[1,2] Hiroyuki OKADA,[1]
Masayuki AKIYAMA,[3] Gavin DALTON,[4,5] Karl GLAZEBROOK,[6]
Fumihide IWAMURO,[7] Toshinori MAIHARA,[7] Kouji OHTA,[7] Ikkoh SHIMIZU,[1]
Naruhisa TAKATO,[8] Naoyuki TAMURA,[9] Kiyoto YABE,[10]
Andrew J. BUNKER,[9,12] Jean COUPON,[11] Pedro G. FERREIRA,[12]
Carlos S. FRENK,[13] Tomotsugu GOTO,[14] Chiaki HIKAGE,[15]
Takashi ISHIKAWA,[7] Takahiko MATSUBARA,[15] Surhud MORE,[9]
Teppei OKUMURA,[9] Will J. PERCIVAL,[16] Lee R. SPITLER,[17,18]
and Istvan SZAPUDI[19]**

[1] Department of Astronomy, School of Science, The University of Tokyo, 7-3-1 Hongo, Bunkyo-ku, Tokyo 113-0033, Japan
[2] Research Center for the Early Universe, School of Science, The University of Tokyo, 7-3-1 Hongo, Bunkyo-ku, Tokyo 113-0033, Japan
[3] Astronomical Institute, Faculty of Science, Tohoku University, 6-3 Aramaki, Aoba-ku, Sendai, Miyagi 980-8578, Japan
[4] Astrophysics, Department of Physics, Keble Road, Oxford OX1 3RH, UK
[5] RALSpace, STFC Rutherford Appleton Laboratory, HSIC, Oxford OX11 0QX, UK
[6] Centre for Astrophysics & Supercomputing, Swinburne University of Technology, P.O. Box 218, Hawthorn, VIC 3122, Australia
[7] Department of Astronomy, Kyoto University, Sakyo-ku, Kyoto 606-8502, Japan
[8] Subaru Telescope, National Astronomical Observatory of Japan, 650 North A‘ohoku Pl., Hilo, Hawaii 96720, USA
[9] Kavli Institute for the Physics and Mathematics of the Universe (WPI), Todai Institutes for Advanced Study,
the University of Tokyo, 5-1-5 Kashiwanoha, Kashiwa, Japan 277-8583
[10] National Astronomical Observatory of Japan, Mitaka, Tokyo 181-8588, Japan
[11] Astronomical Observatory of the University of Geneva, ch. d’ Ecogia 16, 1290 Versoix, Switzerland
[12] Department of Physics, University of Oxford, Denys Wilkinson Building, Keble Road, Oxford, OX13RH, United Kingdom
[13] Institute for Computational Cosmology, Department of Physics, University of Durham, South Road, Durham, DH1 3LE, UK
[14] Institute of Astronomy, National Tsing Hua University, No. 101, Section 2, Kuang-Fu Road, Hsinchu, Taiwan 30013
[15] Kobayashi-Maskawa Institute for the Origin of Particles and the Universe (KMI), Nagoya University, 464-8602, Japan
[16] Institute of Cosmology and Gravitation, Portsmouth University, Dennis Sciama Building, PO1 3FX, Portsmouth, UK
[17] Australian Astronomical Observatory, PO Box 915, North Ryde, NSW 1670, Australia

[18]Department of Physics & Astronomy, Macquarie University, Sydney, NSW 2109, Australia
[19]Institute for Astronomy, University of Hawaii, 2680 Woodlawn Drive, Honolulu, HI, 96822, USA

*E-mail: tonegawa@astron.s.u-tokyo.ac.jp

Received ; Accepted

Abstract

FastSound is a galaxy redshift survey using the near-infrared Fiber Multi-Object Spectrograph (FMOS) mounted on the Subaru Telescope, targeting Hα emitters at $z \sim 1.18$–1.54 down to the sensitivity limit of Hα flux $\sim 2 \times 10^{-16}\ \mathrm{erg\ cm^{-2} s^{-1}}$. The primary goal of the survey is to detect redshift space distortions (RSD), to test General Relativity by measuring the growth rate of large scale structure and to constrain modified gravity models for the origin of the accelerated expansion of the universe. The target galaxies were selected based on photometric redshifts and Hα flux estimates calculated by fitting spectral energy distribution (SED) models to the five optical magnitudes of the Canada France Hawaii Telescope Legacy Survey (CFHTLS) Wide catalog. The survey started in March 2012, and all the observations were completed in July 2014. In total, we achieved 121 pointings of FMOS (each pointing has a 30 arcmin diameter circular footprint) covering 20.6 deg^2 by tiling the four fields of the CFHTLS Wide in a hexagonal pattern. Emission lines were detected from $\sim 4,000$ star forming galaxies by an automatic line detection algorithm applied to 2D spectral images. This is the first in a series of papers based on FastSound data, and we describe the details of the survey design, target selection, observations, data reduction, and emission line detections.

Key words: techniques: spectroscopic — surveys — galaxies: distances and redshifts — cosmology: large-scale structure of universe — cosmology: observations

1 Introduction

High precision cosmological observations, such as the distance-redshift relations obtained using type Ia supernovae and baryon acoustic oscillations, the anisotropy of the cosmic microwave background, and the large scale clustering of galaxies have established the ΛCDM model (a universe with a non-zero cosmological constant Λ and cold dark matter) as the best description of our expanding Universe (see e.g., Peebles & Ratra 2003; Frieman, Turner, & Huterer 2008; Weinberg et al. 2013; Planck Collaboration et al. 2014). This result emerges from the fact that the Universe experienced a transition from decelerating to accelerating expansion around $z \sim 1$. The origin of this unexpected acceleration is one of the greatest problems in physics and astronomy. It may be a result of an exotic form of energy with negative pressure, Λ being one example, but the problems of its smallness and fine tuning still remain unsolved. Another possibility is that the general theory of relativity (GR) is not adequate to describe the dynamics of spacetime on cosmological scales. If this is the case, we expect the growth rate of large scale structure to show a deviation from the GR prediction. Therefore measurements of the growth rate of structure at various redshifts provides a good test of this hypothesis.

One important observable for measuring the growth rate is the redshift space distortion (RSD) effect in galaxy redshift surveys. Galaxy 3D maps constructed using redshift-space distances are distorted with respect to those in real-space due to the line-of-sight component of the peculiar velocities of galaxies (Kaiser 1987). Isotropic statistics in real-space, such as the two-point correlation function or the power spectrum, develop an apparent quadrupole anisotropy in redshift space, the magnitude of which is sensitive to the velocity power spectrum whose amplitude depends on the quantity $f\sigma_8 = d\sigma_8/d(\ln a)$. Here a is the scale factor of the Universe and σ_8 is the rms amplitude of density fluctuations smoothed by a top-hat filter with a comoving radius of $8h^{-1}$ Mpc. The growth rate is well approximated by $f(z) \sim \Omega_m(z)^\gamma$ where γ is referred to as the growth index parameter and Ω_m is the dimensionless matter density. The value of $\gamma = 0.55$ in GR, while other gravity theories predict different values of γ (Linder 2005). Comparison between the observed value of $f\sigma_8$ and its theoretical prediction at various redshifts is a good test of GR on cosmological scales (Song & Percival 2009), assuming that galaxy biasing is linear. This test has already been performed at $z < 1$ using data from a number of galaxy redshift surveys (Hawkins et al. 2003; Guzzo et al. 2008; Blake et al. 2011; Samushia et al. 2012; Reid et al. 2012; Beutler et al. 2012; **?**; Beutler et al. 2014). The standard ΛCDM model is found to be consistent with the observed values of $f\sigma_8$ and its evolution.

A next important step for this test is to reduce the statistical error on $f\sigma_8$ using larger galaxy surveys at $z < 1$, or to extend the $f\sigma_8$ measurements to even higher redshifts. At higher redshifts, nonlinearities on the physical scales of interest are smaller than they are today, which can result in a cleaner measurement of $f\sigma_8$. Moreover, at high redshifts, $f \sim 1$, and RSD is directly sensitive to σ_8, thus providing a baseline for lower redshifts measurements. RSD has been detected at $z \sim 3$ using Lyman-break galaxies (Bielby et al. 2013), at the significance of $\sim 2\sigma$ level. The principal aim of the FastSound[1] galaxy redshift survey is to measure $f\sigma_8$ at $z \sim 1.18$–1.54 for the first time by detecting RSD using the near-infrared Fiber Multi-Object Spectrograph (FMOS) mounted on Subaru Telescope.

The FMOS instrument has 400 fibers in a 30-arcmin diameter field-of-view, and covers the wavelength range 0.9–1.8 μm in its low-dispersion mode; for FastSound we use the higher-throughput higher dispersion mode working in the H-band and covering 1.43–1.67μm. This allows us to reach the $z > 1$ universe by detecting bright Hα $\lambda 6563$ emission lines from star-forming galaxies. FMOS uses a novel fiber positioning system, called “Echidna”, which is driven by a saw-tooth voltage pulse sent to the piezoelectric actuator, in order to populate 400 fibers in a limited space of 15 cm diameter. The atmospheric OH emission lines are hardware-blocked using an OH mask mirror, thus eliminating a dominant noise source in the near-infrared region.

All the FastSound observations have been completed as the Subaru Strategic Program for FMOS (PI: T. Totani), using 35 nights from March 2012 to July 2014. About $4,000$ emission line galaxies were detected with $S/N \geq 4.0$ in the total survey area of 20.6 deg^2 [121 FMOS field-of-views (FoVs)], and more than 90% of them are considered to be Hα emitters with a median redshift of $z \sim 1.4$. It is expected that RSD will be detected at $\sim 4\sigma$ level from this data set (Paper IV, Okumura et al., in preparation). In addition to enabling a RSD measurement for cosmology, this sample will also provide fresh insights into the evolution of the star formation and metallicity of galaxies at intermediate redshift.

In this paper, we present an overview of FastSound, especially focusing on the survey design, the details of observations and data reductions. We describe the observed survey fields in §2, and the target selection based on photometric redshift and Hα flux estimates in §3. In §4, we present details of our FMOS spectroscopic observations. This is followed in §5 by a description of the data processing using the standard FMOS data reduction pipeline (FIBER-pac; Iwamuro et al. 2012) and automated emission line search by the software FIELD (Tonegawa et al. 2014b). Finally, we present a brief summary in §6. Throughout this paper, all magnitudes are given in the AB system, and coordinates in the equinox J2000.0 system. We adopt a standard set of the cosmological parameters: $(\Omega_m, \Omega_\Lambda, h) = (0.3, 0.7, 0.7)$, where h is $H_0/(100\,\mathrm{km/s/Mpc})$.

2 Survey Fields

The spectroscopic targets for FastSound were selected from the four fields (W1–W4) of the Canada-France-Hawaii Telescope Legacy Survey (CFHTLS) Wide Fields which cover an area of ~ 170 deg^2 in total with five optical band filters of u^*, g', r', i', z' (Goranova et al. 2009). FastSound spans a total of 20.6 deg^2 in these fields. Figure 1 shows the FastSound footprints in the four fields. The FastSound observation regions were chosen so as to maximize its legacy value (i.e., overlap with existing data). In CFHTLS W1, the survey data of HiZELS (Geach et al. 2008; Sobral et al. 2009), SXDS (Furusawa et al. 2008), UKIDSS-DXS and UDS (Lawrence et al. 2007), VVDS Deep (Le Fèvre et al. 2005) and Wide (Garilli et al. 2008), VIPERS (Guzzo et al. 2014), and CFHTLS Deep 1 Field overlap with FastSound. Similarly, the FastSound region in W3 overlaps with the DEEP3 (Cooper et al. 2011) field, and that in W4 overlaps with the UKIDSS-DXS and VVDS Wide fields. Such overlaps would be useful to better understand the physical properties of emission line galaxies detected by FastSound [e.g., stellar mass from NIR data, see Paper III (Yabe et al. 2015) for a study of the mass-metallicity relation].

For FastSound, we adopted a gapless tiling pattern of hexagons inscribed in the FMOS circular FoV of 30 arcmin diameter, as illustrated in Figure 1. The differences of RA and DEC between two neighboring hexagons satisfy Δ(RA) cos(DEC) = $\sqrt{3}r$ and Δ(DEC) = $(3/2)r$, where $r = 0.25$ deg is the radius of the FMOS FoV. The FastSound FoV-ID is related to the central point coordinates by the running integers i and j such that

$$\mathrm{FoV\ ID\ number} = A_k i + j + B_k \tag{1}$$

$$\mathrm{DEC} = d_k - \frac{3}{2} r i \tag{2}$$

$$\mathrm{RA}' = r_{1,k} + \sqrt{3} r j \pm \frac{\sqrt{3}r}{2}\delta_i \quad (+\mathrm{:W1,W4},\ -\mathrm{:W2,W3}) \tag{3}$$

$$\mathrm{RA} = r_{2,k} + \frac{\mathrm{RA}'}{\cos(\mathrm{DEC})} \tag{4}$$

where $\delta_i = 0$ (for even i) or 1 (for odd i), A_k and B_k are integers, while d_k, $r_{1,k}$, and $r_{2,k}$ are non-integers. These are defined in Table 1 for the k-th field of CFHTLS-W ($k = 1$–4). The ranges of i and j are also given in the Table. Because A_k means the number of grids in j (i.e., $j_{\mathrm{max},k} - j_{\mathrm{min},k} + 1$), one can calculate RA and DEC if the field ID number is given, by finding i and j as the quotient and remainder of (ID $-B_k$) divided by

---

[1] The name is composed of two acronyms: one a Japanese name “FMOS Ankoku Sekai Tansa” (FMOS ŁET, meaning FMOS dark Universe survey), and the other an English name “Subaru Observation for Understanding the Nature of Dark energy”.

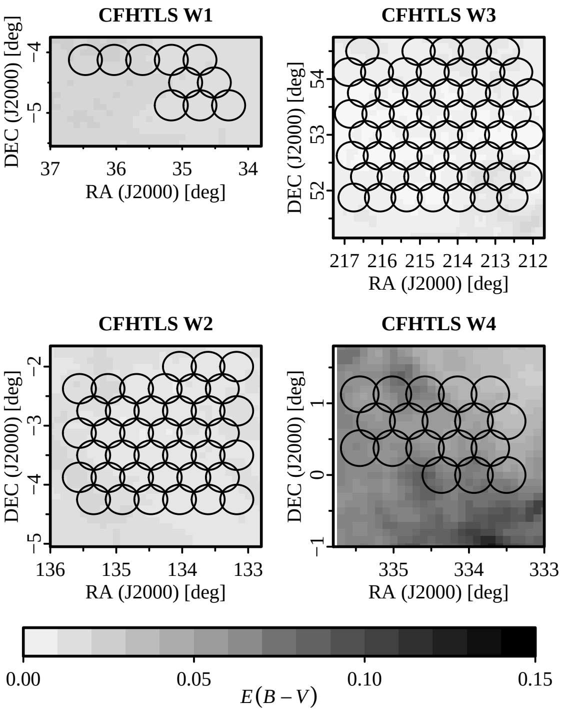

Fig. 2. The Galactic extinction map [$E(B-V)$ from Schlegel et al. 1998] in each of the four FastSound survey fields.

A_k. The FastSound FMOS FoVs are then specified by the field ID (W1–4) and the FoV ID; for example, the W1_030 FoV has $i=1$ and $j=9$, and its central coordinates are (RA, DEC) = (34.5137, -4.5000) in degrees.

The survey was originally planned to cover approximately the same area for the four fields of W1–4, but because of weather conditions and/or telescope/instrument problems, there is a considerable difference in the areas actually observed in each of the fields: 10, 39, 54, and 18 FoVs in the W1–4 fields, respectively. The footprints of FastSound observations are indicated in Figure 1, with different colors for different FastSound observing runs.

3 Target Selection

After an examination of various selection methods for FastSound (Tonegawa et al. 2014a), we chose the photometric redshift and star formation rate estimate based on SED fittings to the five CFHTLS-W optical bands as the FastSound target selection criteria. We started from the z-band selected CFHTLS galaxy catalog produced by Gwyn (2012). We used the MAG_AUTO magnitudes, and the limiting magnitudes are 26.0, 26.5, 25.9, 25.7, and 24.6 for $u^*g'r'i'z'$ respectively at 50% completeness level for point sources (Gwyn 2012). Magnitudes corrected for the Galactic extinction using the $E(B-V)$ map of Schlegel et al. (1998) were used in the following procedures of target selection. The extinction maps in the FastSound survey regions are displayed in Figure 2. The W4 field has higher extinction ($E(B-V)=0.065$ on average) than the other fields ($E(B-V)=0.012$–0.024 on average).

We used the official CFHTLS photometric redshifts ($z_{\rm ph}$) provided for galaxies brighter than $i'=24.0$ (Ilbert et al. 2006; Coupon et al. 2009) [2]. We also considered galaxies for which official $z_{\rm ph}$'s are not provided, as potential FastSound targets. We determined the photometric redshifts of these galaxies in the following manner. We used the public code *LePhare* (Arnouts et al. 1999; Ilbert et al. 2006), with the same templates and parameters as those for the CFHTLS official photo-z calculation. Photo-z training (i.e., zero-point correction for the input photometry) was performed using VVDS Deep and Wide data (Le Fèvre et al. 2005; Garilli et al. 2008). *LePhare* provides the best-fit (minimum χ^2) $z_{\rm min}$ and the median of likelihood distribution $z_{\rm med}$ as estimates of $z_{\rm ph}$. While $z_{\rm med}$ was used as the CFHTLS official photometric redshift, $z_{\rm min}$ was adopted for galaxies calculated by us. (We noticed this difference after the survey started.) Galaxies whose photo-z's were calculated by us are relatively faint compared with those with the official CFHTLS photo-z's, comprising 4.7% of all the final FastSound target galaxies and 1.9% of the emission line galaxies detected. The latter fraction is lower than the former, probably because emission lines of fainter galaxies in i' are weaker and hence more difficult to be detected by FMOS.

There is a tight correlation between star formation rate (SFR) and Hα, and Hα is widely recognized as the best star formation rate indicator of galaxies (Kennicutt 1998). Therefore estimates of SFR are also important for efficiently selecting Hα emission line galaxies. However, the SED templates used in the photo-z calculation are empirical ones, and hence cannot be used to infer a SFR. Therefore we have also performed SED fitting with the theoretical PEGASE2 templates (Fioc & Rocca-Volmerange 1999) assuming the Scalo IMF (Scalo 1986) and the solar metallicity, again using *LePhare*, with redshifts fixed at $z_{\rm ph}$ calculated using the empirical templates. Model templates have exponential star formation histories with decaying timescales of 0.1–20 Gyr and ages of galaxies in the range of 0.3–10 Gyr. The extinction is assumed to be the Calzetti law (Calzetti 2000). We then estimated Hα luminosities from SFR and $E(B-V)$ calculated by *LePhare* (best-fit values at the χ^2 minimum), as

$$\log\left(L_{\rm H\alpha}/[{\rm erg/s}]\right) = 40.93 + \log\left({\rm SFR}/[{\rm M_\odot/yr}]\right) \\ -0.4A_{\rm H\alpha}. \qquad (5)$$

The conversion factor 40.93 was derived by comparing the spectroscopic Hα line luminosities of the SDSS galaxies with those estimated by photometric fittings, using the method of Sumiyoshi et al. (2009). The value is different from that of

---

[2] `http://terapix.iap.fr/`

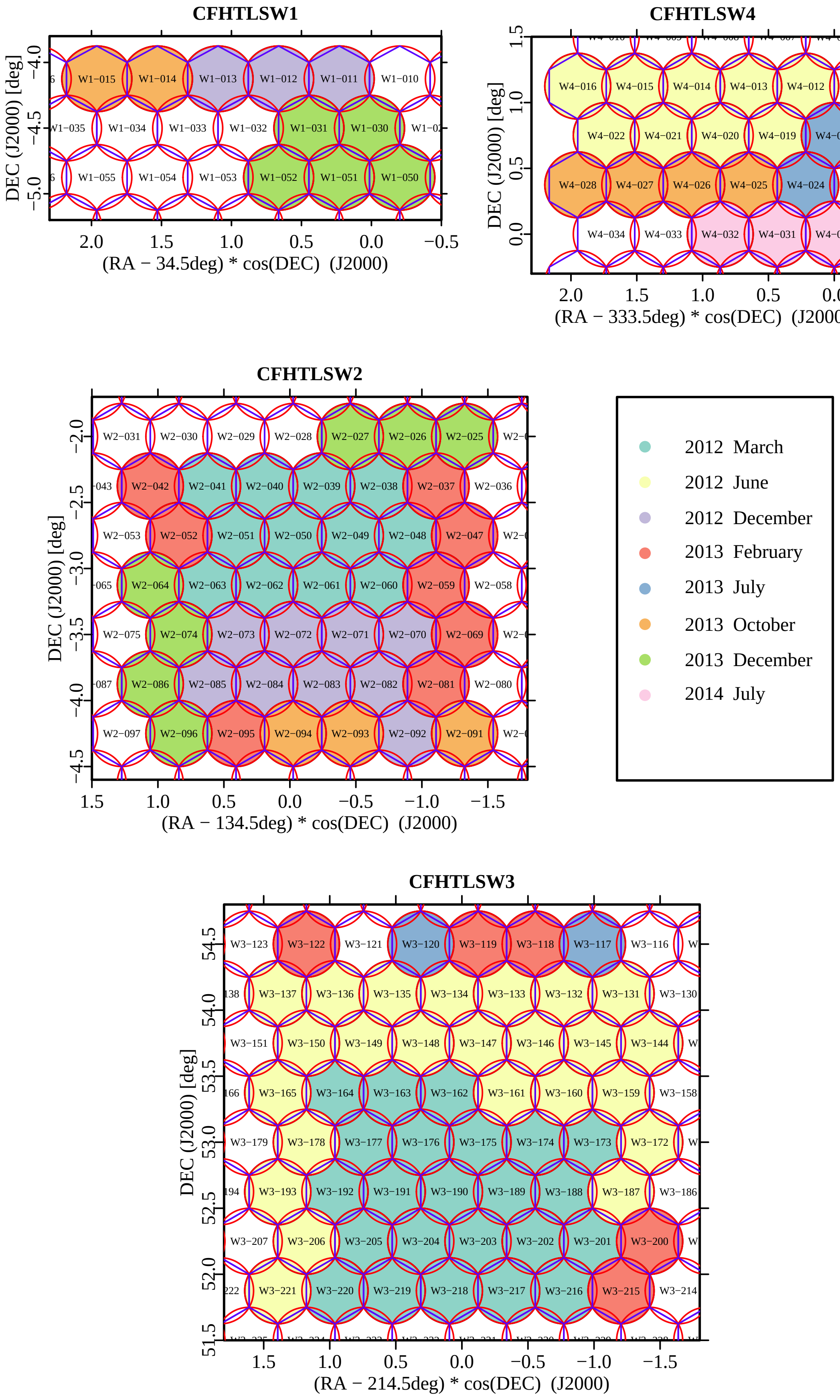

Fig. 1. The footprints of the observed FastSound field-of-views (FoVs). FMOS FoVs (shown by red circles, 30 arcmin diameter) are arranged in a continuous hexagonal tiling. The FMOS FoV field IDs are indicated in each FoV. FoVs actually observed by FastSound are filled by different colors corresponding to different observing periods, as indicated in the figure, while the white FoVs were not observed.

Table 1. The parameters relating the FMOS FoV ID numbers and the central coordinates

k	A_k	B_k	d_k	$r_{1,k}$	$r_{2,k}$	$i_{\rm min}$	$i_{\rm max}$	$j_{\rm min}$	$j_{\rm max}$
1	20	1	-4.125	-4.1	34.5	0	14	0	19
2	11	1	-1.25	-2.19	134.5	0	11	0	10
3	14	1	57.5	-2.72	214.5	0	16	0	13
4	6	6	1.5	0.0	333.5	0	6	-1	4

Note: d_k, $r_{1,k}$, and $r_{2,k}$ are in units of degrees.

Kennicutt (1998) and Sumiyoshi et al. (2009), because of the use of the Scalo IMF rather than the Salpeter IMF. Here, extinction of Hα photons is expected to be larger than that for stellar radiation, and $A_{\rm H\alpha}$ is related to stellar A_V using the prescription discussed in Cid Fernandes et al. (2005). The stellar A_V is estimated from $E(B-V)$ obtained from the SED fitting, assuming the Calzetti law again. Finally $\log L_{\rm H\alpha}$ is converted to Hα flux assuming the photometric redshifts.

We selected galaxies at $1.1 < z_{\rm ph} < 1.6$, according to the redshift range of Hα ($1.18 \le z \le 1.54$) corresponding to the observing wavelength range of FastSound (1.43–1.67 μm using the high resolution mode of FMOS). The range $1.1 < z_{\rm ph} < 1.6$ is wider than the wavelength coverage of FMOS, to allow the $z_{\rm ph}$ range to span the wavelength coverage, including the uncertainties in $z_{\rm ph}$. The typical error, $\sigma_{\Delta z/(1+z_s)} \equiv 1.48 \times {\rm median}(|\Delta z|/(1+z_s))$, is 0.08 for galaxies in our pilot observing run (Tonegawa et al. 2014a).

We further selected galaxies satisfying $20.0 < z' < 23.0$ and $g' - r' < 0.55$; these conditions were introduced to increase the success rate of emission line detection by FMOS, based on past experience (see Tonegawa et al. 2014a). Finally, we set a threshold for the estimated Hα flux, to select a required number of Hα bright galaxies. In FastSound, each FMOS FoV is visited only once with one fiber configuration, and hence the threshold flux is set so that the number of target galaxies within FMOS FoV is about ~ 500, slightly more than the number of FMOS fibers, allowing for dropouts due to the fiber collision or the density contrast of galaxies. A fixed threshold flux is adopted within one of the four CFHTLS Wide fields, but it is different for different fields: 1.0×10^{-16} erg cm^{-1} s^{-1} for W1/W2, 1.1×10^{-16} erg cm^{-1} s^{-1} for W3, and 0.9×10^{-16} erg cm^{-1} s^{-1} for W4. This final galaxy sample within each FMOS FoV is sent to the fiber allocation software of FMOS. (In this work we call this sample as the target galaxies in FastSound, which is different from the galaxy sample that were actually observed by FMOS, because fiber allocation is not complete. See §4.2.) The $u^* g' r' i' z'$ magnitude distribution of the target galaxies and fiber-allocated galaxies compared to all CFHTLS-Wide objects in the survey footprint is displayed in Figure 3. Our target selection is biased towards blue star-forming galaxies, but this is not a serious problem for $f\sigma_8$ measurement within the linear regime, as mentioned in §1.

4 Observations

4.1 Basic Strategy

FMOS has two modes for fiber configuration: the normal-beam switch (NBS) mode and the cross-beam switch (CBS) mode. In NBS mode, all the 400 fibers are allocated to target objects in an on-source exposure, and then the FoV is offset to observe the off-source sky background, with the same fiber configuration. In CBS, on the other hand, the fibers are split into two groups of 200 fibers, and one observes targets while the other observes the sky background. Two exposures are taken for one target set, exchanging the role of two fiber groups. The CBS mode has the advantage of shorter observing time required to achieve a fixed S/N when targets are less than 200 in a FoV. However, CBS has the disadvantage of more complicated fiber configuration, resulting in a smaller number of allocated spines than NBS. Therefore we chose NBS for the FastSound project.

FMOS provides two different spectral resolution modes: the low-resolution (LR) mode and the high-resolution (HR) mode. The LR mode covers 0.9–1.8 μm with a typical spectral resolution of $R \sim 500$, while HR covers a quarter of the wavelength range covered by LR with $R \sim 2200$ where $R = \lambda/\Delta\lambda$ and $\Delta\lambda$ denotes FWHM. The HR mode was chosen for FastSound because in LR the additional volume-phase holographic (VPH) grating used to anti-disperse spectra decreases the instrumental throughput by a factor of about two (Kimura et al. 2010). The wavelength range was set to be $\lambda = 1.43$–1.67 μm (called H short+), corresponding to Hα $\lambda 6563$ at $z = 1.18$–1.54. In the H short+ wavelength range, the spectral resolution changes within the range of $R \sim 2000$–2700, with the typical value of 2400. The detector size is 2k×2k, and hence the pixel scale is ~ 1.1 Å/pix.

The FastSound survey observed each FMOS FoV with a single set of fiber configuration including ~ 400 targets, selected by the procedures described in the previous section. The light from the targets collected by the 400 fibers of FMOS is sent to the two spectrographs, IRS1 and IRS2, each of which produces about 200 spectra. For each FoV we observed two sets of 15 min on-source and 15 min off-source, i.e., total 30 min on source. Including 30 min of overhead, each FoV typically took about 90 min, allowing us to observe about 6 FoVs per night. Sometimes three or more source frames were taken in one FoV,

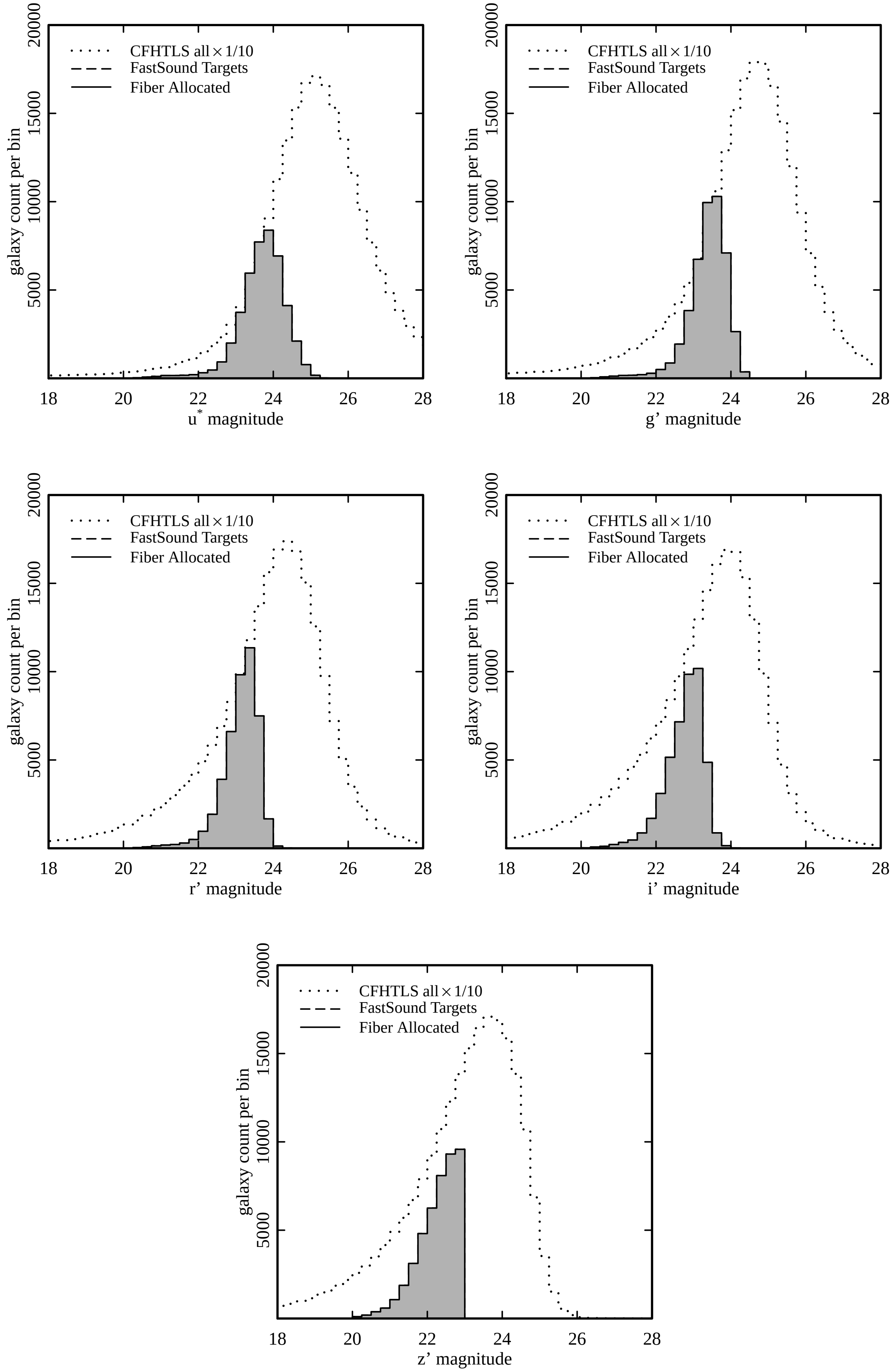

Fig. 3. The histogram of $u^* g' r' i' z$ magnitudes of all CFHTLS Wide galaxies in the FastSound footprints (dotted), FastSound target galaxies (dashed), and galaxies that the fibers were actually allocated to (solid). The cutoff of z'-magnitude at 23.0 is due to our selection condition.

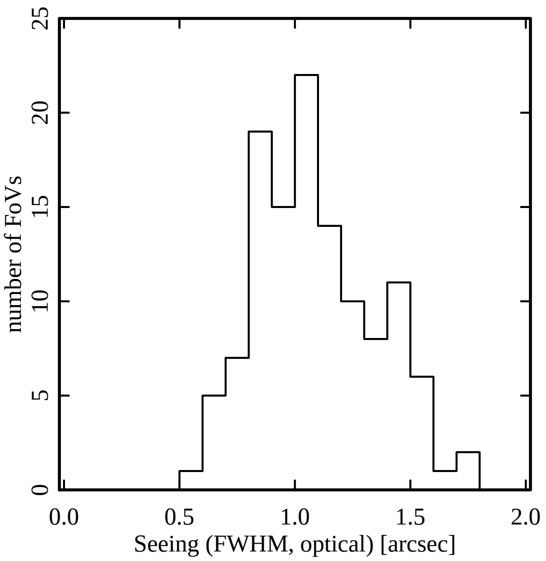

Fig. 4. The histogram of seeing (FWHM) for all the FMOS FoVs in the FastSound survey.

depending on the quality of the data affected by weather conditions.

Seeing was measured during the observing time for each FoV, using an optical image of coordinate calibration stars (see §4.2) taken by the sky camera (CCD camera in the Echidna Focal Plane Imager). The seeing in the FastSound data ranges from ~ 0.6 to $1.6\,\mathrm{arcsec}$ with a mean of $\sim 1.0\,\mathrm{arcsec}$ in FWHM, as seen in Figure 4.

4.2 Fiber Allocation Procedures

Fibers were allocated to the selected targets using the software Spine-to-Object (S2O, version 20101007). S2O takes ".fld" files prepared by users with the coordinate list of science targets as input and produces ".s2o" files as outputs containing the allocation results. In addition to science targets, several types of stars need to be included in the .fld files: guide stars, coordinate calibration stars (CCS), and flux calibration stars (FCS). We used the Two-Micron All-Sky Survey (2MASS) point sources catalog (Cutri et al. 2003) with available NIR magnitudes for these stars. To reduce the systematic uncertainties about the coordinates given in 2MASS and CFTHLS, we examined the cross-matched objects between the two, and found systematic offsets (typically ~ 0.07 arcsec, depending on the four fields of W1–4) between the coordinates reported by these two surveys. These offsets reduce the number of cross-matched stars, and hence this offset was corrected for each of the four fields, and the cross-match was taken again. The random errors for individual objects between the two systems are typically ~ 0.2 arcsec. We used these cross-matched objects as the star sample for all FastSound observations, using the CFHTLS coordinates for them to be consistent with target galaxies.

FMOS requires at least three guide stars near the edge of the FoV, and they should be bright in optical bands. We selected guide stars which satisfy the following conditions: (i) $11.5 < z' < 15.4$, (ii) $11.5 < R < 15.5$, and (iii) located at 0.22–$0.30\ \mathrm{deg}$ from the center of a FoV. Typically 3–6 guide stars were selected in the final s2o output. Guide stars are observed by dedicated guide fibers of FMOS, and they do not affect the number of scientific targets. Coordinate calibration stars (CCS) were used to correct the rotational offset of FoV. We selected ~ 5 CCSs close to the center of FoV and ~ 10 distant from the center. CCSs in the outer regions provide an efficient rotational calibration, while CCSs near the FoV center are used for focusing. The sky camera takes the image of CCSs and hence no fibers need to be reserved for these stars. The selection criteria for the CCSs were (i) $11.5 < z' < 15.4$ and (ii) $11.5 < R < 15.5$. Faint stars (15–18 mag in JH bands) are needed as FCSs for spectral calibration of science targets. We allocated about eight fibers to FCSs (i.e., four stars for each of IRS1 and IRS2), which are the same fibers as those for scientific targets. The selection criteria were (i) $0.3 < g' - r' < 0.5$, (ii) $16.5 < r' < 18.0$, and (iii) $H > 16.25$. These conditions were driven by the desire to select G type stars for calibration as they have flat spectra and do not have strong absorption lines in H band.

The parameters adopted in the S2O software are as follows. The beam-switch offset was set to be $(10, 0)\ \mathrm{arcsec}$ in the Echidna system coordinates. The target priority ("1"=highest and "9"=lowest) was set to "1" for guide stars and "3" for other objects. Another important parameter for fiber allocation is position angle (PA) of FoV relative to the celestial sphere. For each FoV, we tried various PAs to find the best one, for stable guiding (i.e., a sufficient number of guide stars) and to maximize the number of science target galaxies. For each FoV we checked that roughly equal numbers of FCSs were included for IRS1 and IRS2 fibers, and that the FCS fibers were not at edge of the detectors, to avoid a decrease of flux calibration accuracy. We accepted redundant observations and we did not omit galaxies at the edge of FoV from our target list, even if they were already observed by an adjacent FoV.

Typically we allocated ~ 360 fibers to objects, although there are ~ 400 fibers and ~ 500 targets within a FoV, which is mainly due to the fiber collision and non-uniform distribution of galaxies on the sky. This is illustrated in Figure 5 as a histogram of the fiber allocation percentage relative to the number of target galaxies selected by the FastSound selection condition (§3). The home positions of FMOS fibers are in a regular triangular lattice pattern with the fiber spacing of $84''$, and there is no inaccessible area in the FoV because the patrol area of the fibers is $87''$ arcsec in radius. However, the minimum allowed separation between neighboring fibers is $12''$ arcsec. Therefore

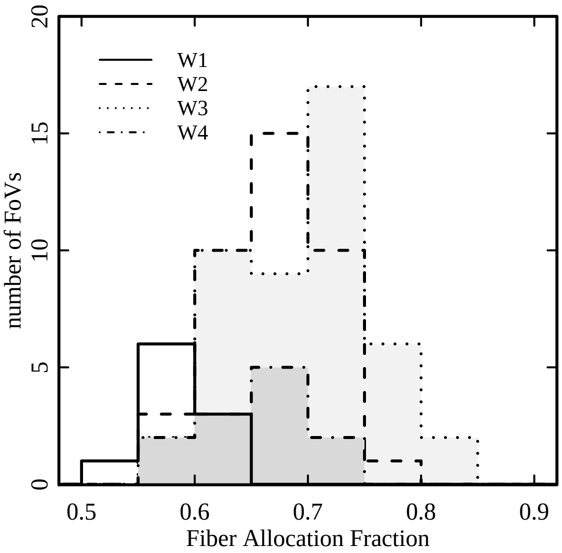

Fig. 5. The histogram of the fraction of fiber-allocated galaxies in those selected as the FastSound target galaxies in §3.

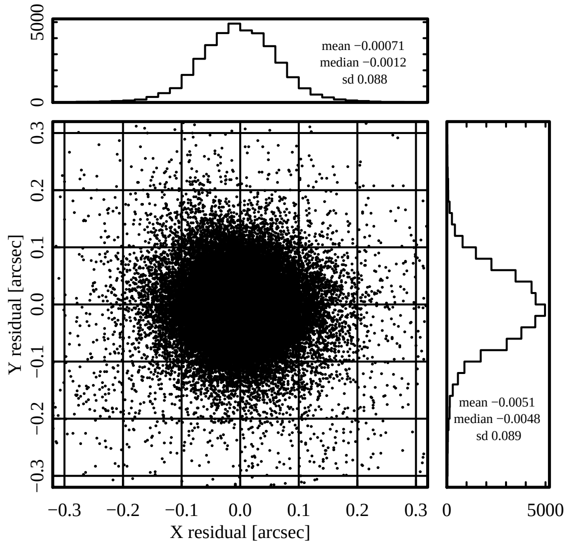

Fig. 6. The fiber pointing accuracy for the FastSound scientific target galaxies, showing the residual between the actual fiber positions and input coordinates of targets.

spines cannot be allocated to a pair of galaxies if they are closer than $\sim 12''$ arcsec. This effect will be taken into account in the clustering analysis reported in the forthcoming FastSound papers.

Figure 6 shows the accuracy of fiber allocation to targets, derived as the difference between input fiber positions in the ".s2o" files and those recorded during observations. The offset is within 0.12 arcsec for almost all targets, which is consistent with the designed performance of the Echidna system (Kimura et al. 2010).

4.3 A Note on OH Masks

The OH mask mirrors are an important feature of FMOS and are used to suppress the strong OH airglow in the near-infrared bands. When the FastSound observations started (Mar. 2012), two different mask mirrors were used for IRS1 and IRS2, made by different techniques: thin stainless steel wires were placed at the positions of OH airglow lines for IRS1, while the mirror of IRS2 was directly coated with reflective gold. There was also a difference of the masked wavelength regions between the two; the mask mirror of IRS2 masked fewer OH lines than that of IRS1, because the former did not cover some faint OH lines. It was found that the IRS2 mask worked better and was more stable than IRS1, because the steel metal was sensitive to minute-scale changes of temperature in the refrigerator. Therefore the IRS1 mask mirror was replaced with that masking the same wavelength regions and made by the same technique as IRS2 in an engineering run conducted in Sep 7–9 2012, i.e., during the 2-year FastSound observation campaign. This change will be appropriately taken into account in the galaxy clustering analysis. The proportion of the masked wavelength region for IRS1 decreased from 22% to 10% in the whole FMOS wavelength range in LR, and from 27% to 16% in the HR wavelength range (H short+) used for FastSound, by this upgrade.

5 Data Reduction

The FastSound data were reduced with the FMOS data reduction pipeline (FIBRE-Pac: Iwamuro et al. 2012). The software performs relative flux (i.e., spectral shape) calibration by choosing one of the flux calibration stars clearly seen on the 2D image in a FoV. The line flux reported in the FastSound catalog is calculated from the observed counts of the final spectral data produced by FIBRE-Pac, where the counts are normalized so that 1 count per pixel corresponds to 1μJy. It should be noted that this absolute flux normalization is not calibrated by FCSs, but by assuming a fixed total throughput of 5% (in the HR mode) obtained in good observing conditions (Iwamuro et al. 2012). Varying observational conditions and the fiber aperture effect against point sources can be corrected by the quantity $f_{\rm obs}$, which is defined as the ratio of the flux calculated by FIBRE-Pac for a FCS to that reported in the 2MASS catalog. There is typically $\sim 20\%$ scatter in $f_{\rm obs}$ for individual FCSs within a FoV, caused mainly by fiber positioning errors and chromatic and/or instrumental aberrations. The average of $f_{\rm obs}$ within each FMOS FoV ($\langle f_{\rm obs}\rangle$) was calculated and included in the FastSound catalog. In Figure 7, we show the distribution of $\langle f_{\rm obs}\rangle$ of all the FastSound FoVs, whose average is ~ 0.6. The total flux from a point source can be estimated by dividing the line flux in the FastSound catalog by $\langle f_{\rm obs}\rangle$, but for extended sources, an additional correction for the fiber aperture effect would be required to estimate the total flux. The detailed procedure to convert the uncalibrated flux in the catalog to the calibrated total flux from emission line galaxies will be described in Paper II (Okada et al. 2015).

Emission lines were searched for automatically using the software, FMOS Image-based Emission Line Detection (FIELD), developed for the FastSound project (Tonegawa et al. 2014b). We briefly summarize the algorithm here. The continuum component is first subtracted from the 2D spectral image. Then the 2D image is convolved with a 2D Gaussian kernel that has a similar wavelength and spatial dispersion to the typical line profile of star forming galaxies. The line signal-to-noise is calculated by this convolved flux and its error, and the peaks are searched along the wavelength direction. Special care needs to be taken to reduce the number of false detections in the neighborhood of the OH mask regions, which is especially important for a line search in the FMOS data. Peaks with S/N larger than a given threshold are selected as the line candidates.

In order to avoid multiple detections from one emission line, we set the minimum separation of candidates to be 20 pix along the wavelength direction. If there were more than two S/N peaks within this separation, we selected the one with the largest S/N as a line candidate. The 20 pix scale corresponds to $\sim 440{\rm km/s}$, and therefore emission lines of normal galaxies with a velocity dispersion of $\lesssim$ 200 km/s should not be blended with neighboring line candidates. Finally, we removed a small fraction of objects from the candidate sample, by using some 2D shape parameters indicating that they are spurious objects.

In this way we detected $4,797$ emission line candidates at $S/N \geq 4.0$ in all the FastSound data set (see Table 2 and Figure 8 for the dependence on S/N). It should be noted that the number of galaxies hosting these candidates is $4{,}119$, because ~ 200 galaxies are detected with more than two different lines (see Paper II, Okada et al. 2015), and ~ 400 galaxies are detected in two different FastSound FoVs because they were observed twice in the regions of two overlapping FMOS FoVs. Typically, the number of detected emission line galaxies in one FMOS FoV is about 10% of the 400 fibers. This relatively low success rate is consistent with that obtained in our pilot observations reported in a previous paper (Tonegawa et al. 2014a). In that paper, we discussed the factors determining the success rate, by checking how Hα emitters found in a narrow-band survey were omitted from the FMOS targets. The main reasons were the uncertainty in the photometric redshift estimates, which is large relative to the FastSound redshift coverage, and the uncertainty in the Hα estimates. There are about 380 Hα emitters in one FMOS FoV whose Hα fluxes are detectable by FMOS, and hence a detection efficiency close to 100% should be possible, if the target selection is perfect. However, only about $1/3$ of them remain after the photo-z cut, and another $\sim 1/3$ remain after the Hα flux and color cuts, resulting in $\sim 10\%$ detection efficiency.

Table 2. The statistics of the detected line candidates in all the FastSound data set.*

	Obj.$-$Sky (1)	Sky$-$Obj. (2)	Contamination (2)/(1)
$S/N \geq 5.0$	$3,080$	72	2.3%
$S/N \geq 4.5$	$3,769$	170	4.5%
$S/N \geq 4.0$	$4,797$	441	9.2%
$S/N \geq 3.5$	$6,805$	$1,510$	22.2%
$S/N \geq 3.0$	$12,795$	$6,279$	49.1%

*Statistics for both the normal (Obj.$-$Sky) and inverted (Sky$-$Obj.) images are presented. The inverted frames should include only spurious objects.

All the $4,797$ line candidates cannot be guaranteed to be real emission lines, as the false line detection rate cannot be reduced to zero. The false detection rate increases with decreasing threshold of the line S/N. We estimated the number of false detections by applying FIELD to inverted images, which are obtained by exchanging object and sky frames in the reduction process. It is expected that the rate of false detection of spurious objects should be the same for the normal (Obj.$-$Sky) and inverted (Sky$-$Obj.) frames, because the analysis procedures are exactly the same except for swapping the object/sky frames. (Absorption lines may appear as emission lines in the inverted frames, but the continuum emission is hardly detected for most of FastSound galaxies and absorption lines are under the detection limit.)

The numbers of detected line candidates in all the FastSound data in normal and inverted frames are summarized in Table 2 and shown as a cumulative histogram of S/N in Figure 8. The contamination of spurious objects is about 10% above $S/N = 4$, and sharply increases for a lower S/N threshold. Therefore the number of real emission lines detected by FastSound can be estimated to be about $4,300$ at $S/N \geq 4$. The 441 lines at $S/N \geq 4$ in the inverted frames are hosted by 398 galaxies, and hence the number of galaxies with real emission lines above this S/N should be $4,119 - 398 \sim 3,700$. More than 90% of these lines are expected to be Hα (Tonegawa et al. 2014a; Paper II).

The wavelength of the detected objects in normal and inverted frames are presented against S/N in Figure 9. Here, the wavelengths were derived by 1D Gaussian fits with a velocity dispersion as a free parameter for detected lines. When an OH mask region is overlapping with a line, the line center may be on the mask region. The number of fake lines on the inverted frames rapidly increases below $S/N = 5.0$, indicating that one should adopt some S/N threshold not to include spurious objects into analysis.

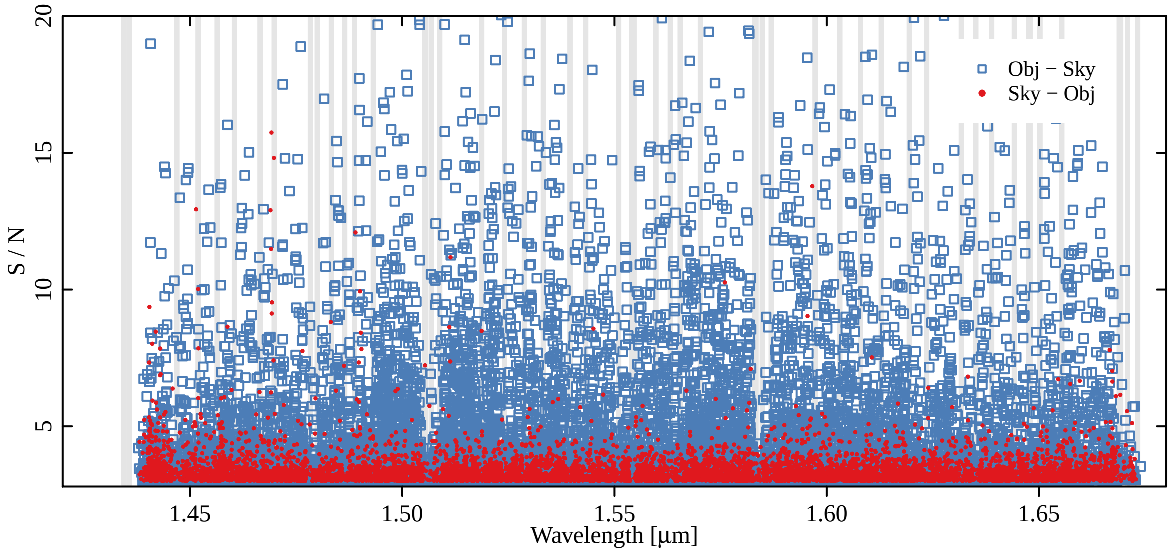

Fig. 9. The S/N of emission line plotted against the observed wavelength. Blue and red symbols represent the detected objects in normal and inverted frames, respectively. Grey vertical stripes show the positions of OH masks of IRS2.

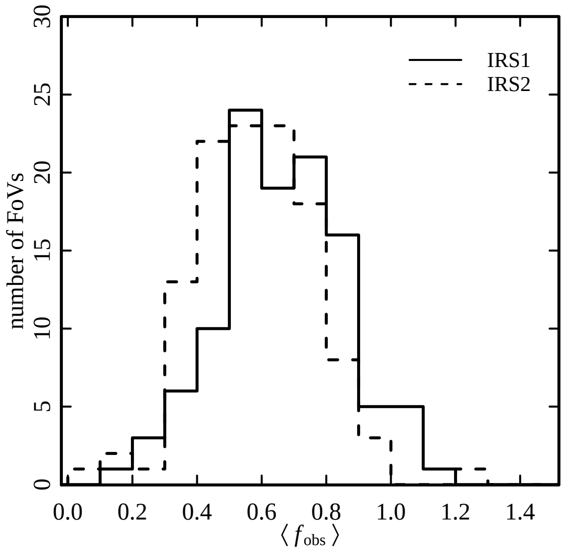

Fig. 7. The distribution of $\langle f_{\rm obs}\rangle$ within each FoV.

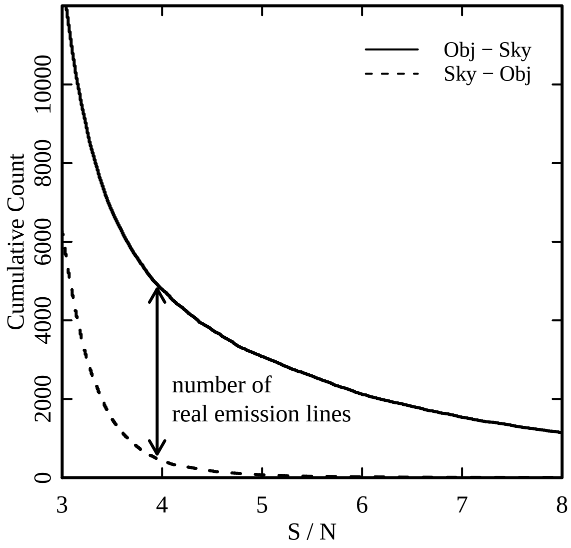

Fig. 8. The cumulative S/N distribution of all the emission line candidates in the FastSound survey. The solid and dashed lines show the number of candidates detected in the normal and inverted frames, respectively. The number of real emission lines can be estimated by the difference between the two.

6 Conclusion

This is the first in the series of papers based on the FastSound project, a cosmological galaxy redshift survey designed to detect redshift space distortions (RSD) in the clustering of galaxies at $z \sim 1.4$. The survey targets Hα emission line galaxies using the near-infrared fiber multi-object spectrograph (FMOS) of the Subaru Telescope, which has a circular FoV with 30 arcmin diameter including 400 fibers. The main scientific goal of the project is to investigate the origin of the accelerated expansion of the Universe and to test General Relativity using a measurement of the growth rate of large scale structure.

In this paper, we presented the survey design, the observation strategy and the basic data reduction adopted by FastSound. We used the CFHTLS Wide catalog in the four fields (W1–W4) to select potential target galaxies, and selected galaxies expected to have high Hα flux based on photometric estimates of redshifts and star formation rates using the five CFHTLS optical bands.

The observations were carried out over 35 nights from April 2012 to July 2014. We observed 121 FMOS FoVs in total (10, 39, 54, and 18 for W1–4, respectively), corresponding to a total area of $20.6\,\mathrm{deg}^2$ tiled with a continuous hexagonal pattern. The data processing was done using the standard FMOS reduction pipeline (FIBRE-Pac) and the automatic line detection software for FMOS (FIELD). We detected $\sim 4,700$ emission line candidates at $S/N \geq 4.0$ corresponding to the line flux sensitivity limit of $\sim 2 \times 10^{-16}$ $\mathrm{erg\ cm^{-2}s^{-1}}$. About 10% of these should be spurious detections, as judged from the statistics using the inverted frames. Removing duplications by multiple lines in a galaxy and by galaxies observed twice, the number of real emission line galaxies is estimated to be $\sim 3,700$ at $S/N \geq 4$. More than 90% of these are considered to be Hα emitters at $z \sim 1.2$–1.5, and most of the non-Hα contaminants are [OIII] emitters at $z \sim 2$ (see Paper II, Okada et al. 2015).

The forthcoming papers will report on the properties of detected emission line galaxies and the FastSound catalog (Paper II, Okada et al. 2015), on metallicity evolution (Paper III, Yabe et al. 2015), on galaxy clustering analyses to derive cosmological constraints (Paper IV, Okumura et al., in preparation), and other topics such as the analysis of halo occupation distribution to determine the relationship between the emission line galaxies and their host halos (Hikage et al., in preparation).

We are grateful to C. Blake for useful discussions. The FastSound project was supported in part by MEXT/JSPS KAKENHI Grant Numbers 19740099, 19035005, 20040005, 22012005, and 23684007. KG acknowledges support from Australian Research Council Linkage International Fellowship grant LX0989763. AB gratefully acknowledges the hospitality of the Research School of Astronomy & Astrophysics at the Australian National University, Mount Stromlo, Canberra where some of this work was done under the Distinguished Visitor scheme. SM and TO were supported by World Premier International Research Center Initiative (WPI Initiative), MEXT, by the FIRST program "Subaru Measurements of Images and Redshifts (SuMIRe)", CSTP.

References

Arnouts, S., Cristiani, S., Moscardini, L., Matarrese, S., Lucchin, F., Fontana, A. & Giallongo, E. 1999, MNRAS, 310, 540
Beutler, F., et al. 2012, MNRAS, 423, 3430
Beutler, F., Saito, S., Seo, H.-J., et al. 2014, MNRAS, 443, 1065
Bielby, R., Hill, M. D., Shanks, T., et al. 2013, MNRAS, 430, 425
Blake, C., et al. 2011, MNRAS, 415, 2876
Calzetti, D., Armus, L., Bohlin, R. C., Kinney, A. L., Koornneef, J. & Storchi-Bergmann, T. 2000, ApJ, 533, 682
Cid Fernandes, R., Mateus, A., Sodré, L., Stasińska, G. & Gomes, J. M. 2005, MNRAS, 358, 363
Cooper, M. C., Aird, J. A., Coil, A. L., et al. 2011, ApJS, 193, 14
Coupon, J, et al. 2009, A&A, 500, 981
Cutri, R. M., Skrutskie, M. F., van Dyk, S., et al. 2003, VizieR Online Data Catalog, 2246, 0
de la Torre, S., Guzzo, L., Peacock, J. A., et al. 2013, A&A, 557, A54
Fioc, M., & Rocca-Volmerange, B. 1999, arXiv:astro-ph/9912179
Frieman, J. A., Turner. M. S. & Huterer, D. 2008, ARA&A, 46, 385
Furusawa, H., Kosugi, G., Akiyama, M., et al. 2008, ApJS, 176, 1
Garilli, B., et al. 2008, A&A, 486, 683
Geach, J. E., Smail, I., Best, P. N., Kurk, J., Casali, M., Ivison, R. J. & Coppin, K. 2008, MNRAS, 388, 1473
Goranova, Y., et al. 2009, http://terapix.iap.fr/cplt/T0006-doc.pdf
Guzzo, L., et al. 2008, Nature, 451, 541
Guzzo, L., Scodeggio, M., Garilli, B., et al. 2014, A&A, 566, A108
Gwyn, S. D. J 2012, A&A, 143, 38
Hawkins, E., et al. 2003, MNRAS, 346, 78
Ilbert, O., et al. 2006, A&A, 457, 841
Iwamuro, F. et al. 2012, PASJ, 64, 59
Kaiser, N. 1987, MNRAS, 227, 1
Kennicutt, R. C., Jr. 1998, ARA&A, 36, 189
Kimura, M. et al. 2010, PASJ, 62, 1135
Lawrence, A., et al. 2007, MNRAS, 379, 1599
Le Fèvre, O., et al. 2005, A&A, 439, 845
Linder, E. V. 2005, Phys. Rev. D, 72, 043529
Okada, H., et al. 2015, submitted to PASJ (Paper II), arXiv:1504.05592
Peebles, P. J. & Ratra, B. 2003, RvMP, 75, 559
Planck Collaboration, Ade, P. A. R., Aghanim, N., et al. 2014, A&A, 571, AA16
Reid, B. A., et al. 2012, MNRAS, 426, 2719
Samushia, L, Percival, W. J & Raccanelli, A 2013, MNRAS, 420, 2102
Scalo. J. M. 1986, FCPh, 11, 1
Schlegel, D. J., Finkbeiner, D. P & Davis, M. 1998, ApJ, 500, 525
Sobral, D., Best, P. N., Geach, J. E., Smail, I, Kurk, J., Cirasuolo, M., Casali, M., Ivison, R. J., Coppin, K. & Dalton, G. B. 2009, MNRAS, 398, 75
Song, Y.-S., & Percival, W. J. 2009, JCAP, 10, 004
Sumiyoshi, M. et al. 2009, arXiv:0902.2064
Tonegawa, M et al. 2014a, PASJ, 66, 43
Tonegawa, M et al. 2014b, DOI: 10.1093/pasj/psu127
Weinberg, D. H., Mortonson, M. J., Eisenstein, D. J., et al. 2013, Phys. Rep., 530, 87
Yabe, K., et al. 2015, submitted to PASJ (Paper III)